Image-Based Ghost Correction for Interleaved EPI

Michael H. Buonocore* and David C. Zhu

A new image-based ghost correction technique is described for general interleaved EPI. This technique works reliably with both even- and odd-number interleaved EPI sequences. It estimates the phase distortions causing the ghosts as a general function of (*x*,*y*) even in the presence of a significant overlap of parent image and ghosts. If the phase distortion is assumed to be a function of *x* (frequency-encode direction) only, the new technique is similar to a recently published correction method for general interleaved EPI (Hennel. J Magn Reson 1998;134:206–213). However, that study concluded that the method for general interleaved EPI did not work. It showed that the SNRs of the edge pixels were too low to accurately estimate the phase distortion. The new technique utilizes not one, but many pixels in the image for estimating the phase distortion. The technique requires a user-defined ROI to outline the parent image and identify so-called eligible pixels for estimating the phase distortion. When all eligible pixels are used, the SNR of the phase distortion estimate is comparable to that obtained in single-shot EPI. This study provides the first examples of high-quality, image-based correction of multiple ghosts in general interleaved EPI. Magn Reson Med 45:96–108, 2001.

Key words: magnetic resonance imaging; interleaved echo planar imaging; image artifacts; image-based ghost correction

Previously, one of the authors (M.H.B.) published a ghost correction technique (1) based on extracting the spatially dependent phase distortions directly from images reconstructed separately using only the left-to-right traversals of k_x (denoted *l*) or only the right-to-left traversals of k_x (denoted *r*). This method works for single-shot EPI, in which left-to-right and right-to-left echos form an alternating pattern in *k*-space, and Fourier reconstruction produces a single ghost shifted by half the FOV from the location of the parent image. To increase spatial resolution, two or more separate *k*-space traversals (interleaves) can be used to acquire different *k*-space lines that can be combined into one larger data set. This "general interleaved EPI" sequence typically uses an even number of interleaves (2–5), which form a non-alternating pattern of *k*-space lines, as shown in Fig. 1a. Regardless of whether an even or odd number of interleaves are used, a non-alternating pattern of *k*-space lines produces more ghosts, which are more closely spaced in the image. The previously published ghost correction method cannot be applied, because more than one ghost is produced. Phase information from non-k_y encoded reference scans can be used to reduce these ghosts (6–13). However, reference scan correction often does not improve image quality (1,14). The odd-number interleaved EPI was developed specifically to allow high resolution imaging without generating multiple ghosts (15,16). Data from an odd number of interleaves can be combined to form an alternating pattern of *k*-space lines, as shown in Fig. 1b. This alternating pattern cannot be formed using an even number of interleaves. The single N/2 ghost generated can be corrected using the single-shot method in (1).

Hennel (15) derived the extension of the method in Ref. 1 to general interleaved EPI. As in Ref. 1, this correction method assumes that the phase distortions can be represented by a function of *x* only, i.e., $\theta(x,y) = \theta(x)$. For each *x*, the method calls for evaluation of the uncorrected images at a single pixel along the edge of the image, within the ghosts and outside of the parent image. The analysis and experimental data in Ref. 15 showed a poor signal-to-noise ratio (SNR) of the phase distortion estimate, due to inherently low signal intensity along the edge. It showed, however, that if $\theta(x)$ is assumed to be a linear function of *x*, the SNR could be restored.

This study derives a new image-based ghost correction method for general interleaved EPI. The method allows the estimation of a general $\theta(x,y)$, but also extends the method in Ref. 15 for estimation of $\theta(x)$. Ghost correction results for $\theta(x,y) = \theta(x)$, are shown using computer simulated data, real data from a test phantom, and real data from human subject brain studies. Computer simulation is used to predict the error of the phase distortion estimate as a function of object size and number of interleaves. The iterative correction method for $\theta(x,y)$ is verified by numerical simulation, but is not explored further due to the complexity of the global optimization.

The major result of this study is the demonstration that the accuracy of phase distortion estimation, for general interleaved EPI sequences that generate non-alternating *k*-space patterns and multiple closely spaced ghosts, is comparable to that obtained for single-shot and odd-number interleaved EPI sequences that generate an alternating *k*-space pattern and only one N/2 ghost. In particular, the widely used even-number interleaved EPI sequences, which generate non-alternating *k*-space patterns, do not need to be abandoned due to inability to correct the numerous closely-spaced ghosts. This result contradicts the theoretical and experimental results presented in Ref. 15.

METHODS

Theory

Two new methods, one iterative and one non-iterative, for ghost correction for general interleaved EPI are presented below. Detailed derivations are provided in the Appendix. The iterative method is used when the phase distortion is considered to be a general function of *x* and *y*. The non-iterative (i.e., closed form) method is a special case of the iterative method, applicable when the phase distortion is considered to be a function of *x* only.

Ghost-corrected images are defined in the $2h$-element vector of functions $\vec{M}_c(x,y)$ given by

Department of Radiology, University of California–Davis Medical Center, Sacramento, California.

*Correspondence to: Michael H. Buonocore, M.D., Ph.D., Dept. of Radiology, UC–Davis Imaging Center, Rm. 1215, 4701 X Street, Sacramento, CA 95817.

Received 30 March 2000; revised 11 July 2000; accepted 8 August 2000.

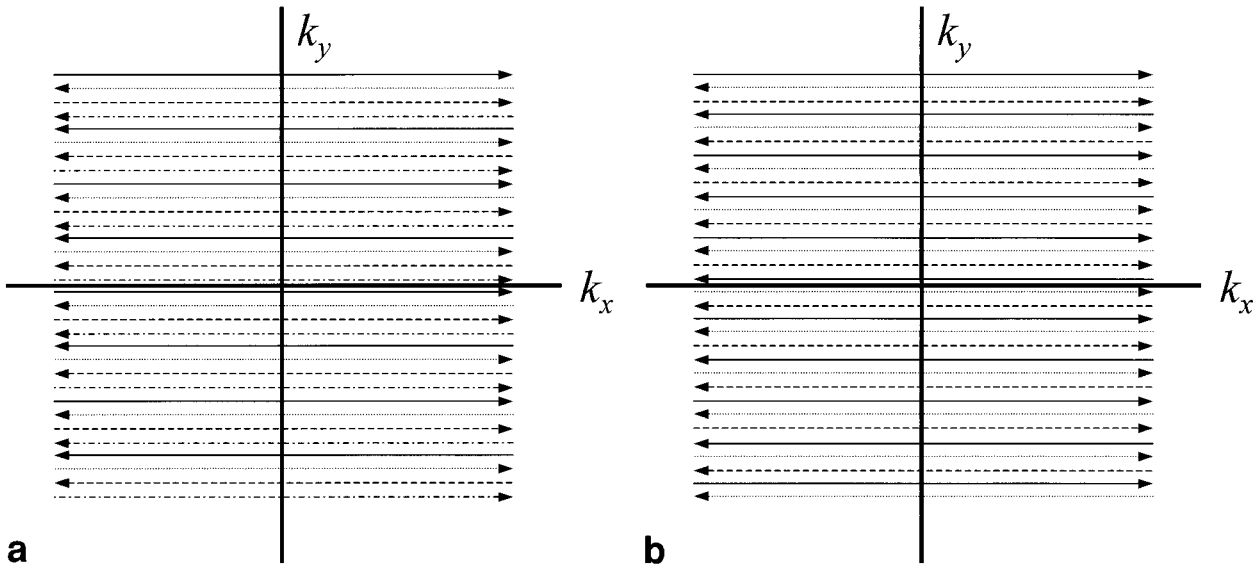

FIG. 1. Example of even- and odd-number interleaved EPI acquisition, showing the fundamental difference in the resulting *k*-space pattern. Each interleaf is identified by a different line: solid, dotted, dashed, and dot-dashed lines, respectively, for the 4-interleaf acquisition, and solid, dotted, and dashed for the 3-interleaf acquisition. Each interleaf acquires lines at equally spaced intervals along k_y, from positive towards negative k_y. The *k*-space pattern is characterized by using "l" to denote a left-to-right traversal along k_x, and "r" to denote a right-to-left traversal. **a:** Four-interleaf EPI acquisition. Each interleaf acquires every fourth line, from a unique starting line at the top. Although an alternating "lrlrlrlr. . ." pattern was sought, the closest that can be achieved is an "lrlrrrlrl. . ." pattern, which has a repeating traversal ("rr" or "ll") every fourth line. **b:** Three-interleaf EPI acquisition. The alternating pattern "lrlrlr. . ." is obtained.

$$[\vec{M}_C(x,\,y)]_j \equiv M_C(x,\,y-\Delta_j) \qquad [1]$$

where $j = 0,1,\ldots,2h-1$, and each entry $M_C(x,y-\Delta_j)$ represents a shifted version of the corrected image, $\Delta_j \equiv jN/2h$, and h is the number of interleaves. $\vec{M}_C$ is partitioned into two h-element vectors according to

$$\vec{M}_C(x,\,y) \equiv \begin{pmatrix} \vec{M}_C^{(1)}(x,\,y) \\ \vec{M}_C^{(2)}(x,\,y) \end{pmatrix} \qquad [2]$$

and these corrected images are calculated from

$$\vec{M}_C^{(1)} = \frac{1}{2h}\exp(-i\Theta^{(1)})(\vec{M}_l^{(1)} + X_l)$$

$$\vec{M}_C^{(2)} = \frac{1}{2h}\exp(i\Theta^{(2)})(\vec{M}_r^{(2)} + X_r) \qquad [3]$$

where $\vec{M}_l(x,y)$ and $\vec{M}_r(x,y)$ are, respectively, vectors of length $2h$ (defined similarly to $\vec{M}_C$) representing the images reconstructed using only the left-to-right, or right-to-left *k*-space lines (with missing lines replaced with zeros). $\Theta(x,y)$ is a $2h \times 2h$ diagonal phase distortion matrix given by

$$[\Theta(x,\,y)]_{i,j} \equiv \theta(x,\,y-\Delta_j) \quad \textit{if } i=j, \quad 0 \textit{ otherwise} \qquad [4]$$

and partitioned according to

$$\Theta(x,\,y) \equiv \begin{pmatrix} \Theta^{(1)}(x,\,y) & 0 \\ 0 & \Theta^{(2)}(x,\,y) \end{pmatrix} \qquad [5]$$

For each (x,y) location, and for any particular Θ, X_l and X_r are calculated from the matrix equations

$$\begin{pmatrix} \exp(i2\Theta^{(1)})U_{11}U_{21}^{-1} & I \\ \exp(i2\Theta^{(2)}) & U_{22}U_{12}^{-1} \end{pmatrix}\begin{pmatrix} X_r \\ -X_l \end{pmatrix} = \begin{pmatrix} I & \exp(i2\Theta^{(1)})U_{12}U_{22}^{-1} \\ U_{21}U_{11}^{-1} & \exp(i2\Theta^{(2)}) \end{pmatrix}\begin{pmatrix} \vec{M}_l^{(1)} \\ -\vec{M}_r^{(2)} \end{pmatrix} \qquad [6]$$

where U_{ij}, $i = 1,2$, $j = 1,2$, are the $h \times h$ sub-blocks of a $2h \times 2h$ discrete Fourier transform matrix, the rows and columns of which are rearranged in accordance with the specific pattern of *k*-space lines. Eqs. [3] and [6], when used with the cost function defined below, constitute an iterative solution to finding the optimal phase distortion estimate of $\theta(x,y-\Delta_j)$ for general interleaved EPI. At each (x,y) location, after X_l and X_r have been solved using Eq. [6] with a particular Θ, Eq. [1] is evaluated to measure how well $\vec{M}_C$ satisfies constraints based on the conditions $M(x,y-k\Delta) = 0$ (where $M(x,y)$ represents the object being reconstructed), for specific integers k. Constraints on $\vec{M}_C$ are met by iteratively searching for Θ that minimizes a positive definite cost function I, which involves $\vec{M}_C$ terms that should equal zero. This cost function is written

$$\mathrm{I} \equiv \vec{M}_C^{\dagger}P_c\vec{M}_C = \vec{M}_C^{(1)\dagger}P_c^{(1)}\vec{M}_C^{(1)} + \vec{M}_C^{(2)\dagger}P_c^{(2)}\vec{M}_C^{(2)} \qquad [7]$$

where P_c is a $2h \times 2h$ diagonal projection matrix with $[P_c]_{kk} = 1$ if $M(x,y-k\Delta) = 0$, 0 otherwise, and $P_c^{(1)}$ and $P_c^{(2)}$ denote the $h \times h$ subblocks on the diagonal of P_c.

Phase distortion that is a function of x only can be represented by $\Theta^{(1)} = \theta_0 I$ and $\Theta^{(2)} = \theta_0 I$, where I denotes

the $h \times h$ identity matrix and θ_0 is a scalar. Substitution of these into Eq. [6] results in the following solution for X_l and X_r:

$$X_r = \exp(-i2\theta_0)\vec{M}_l^{(2)} \quad X_l = \exp(i2\theta_0)\vec{M}_r^{(1)} \qquad [8]$$

Eq. [2] for the corrected images becomes

$$\vec{M}_C^{(1)} = \frac{1}{2h}\exp(-i\theta_0)(\vec{M}_l^{(1)} + \exp(i2\theta_0)\vec{M}_r^{(1)})$$

$$\vec{M}_C^{(2)} = \frac{1}{2h}\exp(i\theta_0)(M_r^{(2)} + \exp(-i2\theta_0)\vec{M}_l^{(2)}) \qquad [9]$$

The Cost function, Eq. [7], can be minimized (set to zero) with

$$\theta_0 = -\frac{1}{2}\arg(w) \qquad [10]$$

where scalar w is defined $w \equiv (\vec{M}_l^{(1)})^\dagger P_c^{(1)}\vec{M}_r^{(1)} + (\vec{M}_l^{(2)})^\dagger P_c^{(2)}\vec{M}_r^{(2)}$ at the (x,y) location. Because this special case assumes that the phase distortion is independent of y, the estimates found at different eligible y locations at each x location are averaged. Changing w to w_y in the definition of w to represent particular y locations, and defining $W \equiv \Sigma_y w_y$, a weighted average phase distortion estimate can be obtained from

$$\theta_0 = -\frac{1}{2}\arg(W) \qquad [11]$$

Eq. [11] constitutes the new closed-form solution to the ghost correction problem.

Eqs. [3], [6], and [7] can be used to correct the image at every (x,y) location. At each x location, they can be solved over a central band of y locations, $-\frac{1}{2}(N/2h) < y \leq \frac{1}{2}(N/2h)$. The equations for a particular (x,y) will use the values of $\vec{M}_l^{(1)}$ and $\vec{M}_r^{(2)}$ at locations $(x,y-k\Delta)$, $k = 0,1,\ldots 2h-1$, and will find the phase distortion estimates at each of these $2h-1$ locations. When using the assumption that the phase distortion is independent of y, only locations satisfying $M(x,y-k\Delta) = 0$, $M_l(x,y-k\Delta) \neq 0$, and $M_r(x,y-k\Delta) \neq 0$, contribute to the cost function (Eq. [7]). These are the so-called "eligible pixels" that contribute to W in the phase distortion estimate in Eq. [11]. Figure 2 illustrates the locations used in Eq. [6] for an $h = 2$ sequence. Locations shifted by an integer multiple of $N/2h$ pixels along y yield cyclically permuted equations, and their solutions are identical those obtained at the unshifted location.

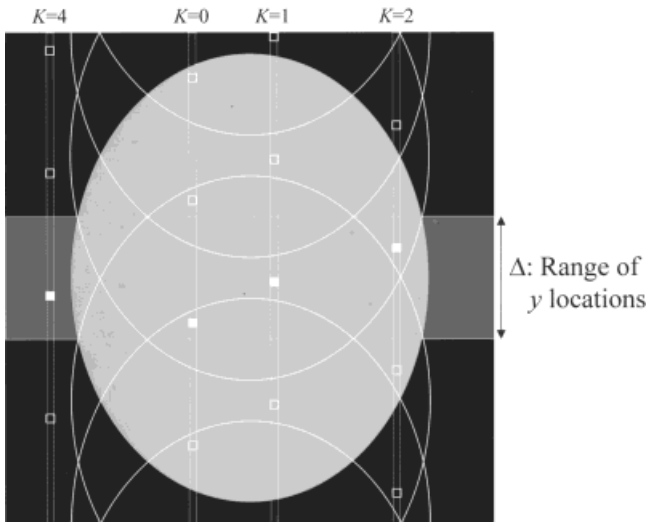

FIG. 2. The (x,y) locations used in the matrix equation in Eq. [6] for a two-interleaf EPI acquisition, are illustrated. The parent image is gray, and the outlines of the four ghosts, each shifted by a multiple of $\Delta = 1/4$ FOV, are shown as white ellipses (with wraparound at the image edge). The vertical arrow identifies the range of (x,y) locations providing unique numerical values for Eq. [6]. Four specific (x,y) locations in that region are marked with solid squares (■). For each specific location, the other (x,y) locations along the vertical, marked with open squares (□) are those used for forming the vectors $\vec{M}_l^{(1)}$ and $\vec{M}_r^{(2)}$ in Eq. [6]. The vertical white lines emphasize that these locations have the same x location. At each specific location, K_θ equals the number of (x,y) locations that lie outside the object, which is also equal to the maximum number of variables allowed in the estimate of $\Theta(x,y)$. The four specific locations were chosen to show different K_θ, but were otherwise arbitrary.

Simulation

The signal and noise associated with phase distortion estimation was investigated using computer simulation, as a function of the size of the object relative to the FOV, and the number of interleaves. The simulation performed reconstruction, in the y-direction only, from raw data corrupted by random noise and phase distortion. It used a 64-point Inverse DFT reconstruction, and assumed that the object was uniform with intensity one, centered in the FOV and covering a specific number of pixels. Phase distortion estimation was investigated for all object sizes from 1 through 63, and with single-shot and 2, 4, 8, and 16 interleaved EPI. Simulated signal from the object was generated using the DFT, and Gaussian random noise was added to the in-phase and quadrature signals, to yield a standard deviation of 0.02 in each of the real and imaginary parts of the reconstructed image. The eligible pixels for phase distortion estimation were determined from the known size of the object.

To compare images with simulation, an approximate relation was derived for the standard deviation σ_θ of the phase distortion estimate θ_0. The standard deviations of the real and imaginary parts of W, both denoted by σ_W, were considered equal, because random noise variances in the in-phase and quadrature channels of the signal were equal. It follows from Eq. [11] that σ_θ is related to σ_W by $\sigma_\theta = \frac{1}{2}\sigma_W/|W|$. Based on Eq. [10] and the definitions below it, random noise σ_M in M_r is multiplied by $M_l^\dagger$ (and vice versa), and these products add incoherently across eligible pixels to determine σ_W. Therefore, for small random noise in the raw data, $\sigma_W \propto |W|^{1/2}$, and it follows that $\sigma_\theta \propto |W|^{-1/2}$. The simulation was designed to confirm the linearity between σ_W^2 and $|W|$.

The dependence of signal and noise on matrix size was also needed. When the number of pixels (with fixed FOV),

and number of raw data points (with fixed bandwidth), are increased in each direction by a factor α,$\alpha > 1$, standard SNR formulas of MRI specify that image intensity in each pixel of $M_l^\dagger$ and M_r will remain unchanged, while σ_M will increase by a factor of α. The number of eligible pixels N_e for θ_0 estimation at each x will increase by a factor of α. Being linear in N_e, W increases by a factor of α. Its standard deviation, σ_W increases by a factor of $\alpha^{3/2}$ (factor of α from σ_M and $\alpha^{1/2}$ from $N_e^{1/2}$). Thus, σ_θ increases as $\alpha^{1/2}$. Note that if in the higher resolution images the number of eligible pixels is increased by summing over adjacent x locations, W increases by a factor of α^2, σ_W increases by a factor of α^2, and σ_θ is unchanged, as expected, because then the net change in image area for θ_0 is unchanged. The average residual of the linear fit of θ_0 across x is expected to increase as $\alpha^{1/2}$, in proportion to the variations of θ_0 at each x.

Computer simulation of 2D interleaved EPI was performed to verify that the proposed technique would correct known phase distortions. A computer program was developed for generating the MRI signal originating from an object constructed as a sum of ellipses (17, 18). The following one-ellipse model was used: ellipse center: (0,0), ellipse radii: 10 cm, 8 cm; ellipse tilt: 0°, with proton density: 1.00 (arbitrary units), and T_2: 100 msec. Interleaved gradient echo EPI was simulated with sampling interval: 8 microseconds; gradient rise time: 56 microseconds (112 microseconds for acquisitions using 256 in frequency-encode direction); FOV: 22 × 22 cm; TE: 40; receiver bandwidth: 62.5 kHz; simulated time delay between left-to-right and right-to-left echo centers: 1.013 sample points; random noise added to data: 0. The only noise in the data was that due to single precision floating point roundoff error of the raw data, and short integer round-off error of the sampled images. Data was acquired with the k-space acquisition pattern of "llrlrlrlrlrlrlrrlrlrlrlrlr-lrlr. . .." This pattern tested the full algorithm in that it necessitated a specific reordering matrix T (see Eq. [A.8]).

Experiments

Gradient recalled interleaved EPI was run on a Signa CV/i 1.5 T MR system (GE Medical Systems, Waukesha, WI) with Version 8.2.5 LX software platform. Even-number interleaved EPI was acquired using an unmodified "epibold" pulse sequence (LX 8.2.5 version, GE Medical Systems, Waukesha, WI). The odd-number interleaved EPI sequence (16) was implemented from this base pulse sequence code. Each interleaf had a relative time delay of the echo center to produce a smooth T_2^* decay as a function of k_y of the combined data set (2).

Scans were performed on a 16.5 cm diameter × 12.3 cm length cylindrical $MgSO_4$-doped water phantom, containing a uniform 9 × 9 grid with horizontal and vertical plastic slats 1.43 cm apart, to evaluate the performance of the ghost correction under conditions in which the ghosts could be relatively easily discerned from the parent image. Interleaved gradient echo EPI was performed with the following common parameters: TR: 2000 msec; FOV: 22 cm × 22 cm; slice thickness: 6 mm; slice spacing: 2 mm; number of slices: 9 (superior 32 mm to inferior 32 mm); flip angle: 90°; number of repetitions: 4; receiver bandwidth: 62.5 kHz; gradient rise time: 56 microseconds (112 microseconds with 256 acquisition); autoshim: off. Even-number interleaved EPI was used to generate the non-alternating k-space patterns: e.g., "llllrrrr. . ." for the 4-interleaf acquisition, "lllllllllrrrrrrrr. . ." for the 8-interleaf acquisition, and "llllllllllllllllrrrrrrrrrrrrrrrr. . ." for the 16-interleaf acquisition. Odd-number interleaved EPI was used to generate the alternating pattern, identical to that obtained in single-shot EPI, e.g., "lr. . .", as previously described (16).

Human imaging was conducted under a research protocol approved by the UC Davis Human Subjects Review Committee, and all subjects gave informed consent. Interleaved gradient echo EPI acquisitions were performed with the following common parameters: TR: 2000 msec; FOV: 22 cm × 22 cm; slice thickness: 6 mm; slice spacing: 2 mm; number of slices: 9 (superior 32 mm to inferior 32 mm); flip angle: 90°; number of repetitions: 4; receiver bandwidth: 62.5 kHz; gradient rise time: 56 microseconds (112 microseconds with 256 acquisition); autoshim: off. Resulting k-space traversal patterns were identical to those described for the phantom.

RESULTS

Experiments

In Table 1, parent image intensity is defined as the average pixel value within an ROI defining the object extent, and ghost intensity by an ROI outside the object, but inside the boundaries of the object projection along the phase-encode direction. Ghost intensity was reported as a percentage of the parent image intensity before correction (column A) and after correction (column B). The quality of ghost correction was measured as ghost intensity after correction, as well as by the percentage reduction of the reported ghost image intensity (column C), i.e., 100*(1 - corrected/uncorrected). The overall phase distortion was determined by a linear least-squares fit of the θ_0 across x (column D). The deviation of θ_0 from a linear function of x was measured as the average absolute value of the linear fit residuals across x (column E). The standard deviation of θ_0 (column F) was computed as the average, across all x locations, of the standard deviation of the θ_0 at each x location across y locations.

Figure 3 shows the (a) uncorrected and (b) corrected reconstruction of the ellipse using the 16-interleaf sequence, with computer simulated data having a relative echo center delay of 1.013 sampling interval. The best-fit linear phase correction was 182.4±0.026° across the FOV (column D, Table 1), in exact agreement with the input delay. Within experimental limits, (b) was a perfect correction, and was verified by reconstructing (without ghost correction) an image (c) using distortion-free simulated data. The linear least square fit was 0.028±0.025° across the FOV. Figure 4 shows the uncorrected and corrected reconstructions of the test phantom using (a) 4, (b) 16, (c) 8, and (d) 9-interleaf axial EPI acquisitions, with phase encoding in the R/L direction. Ghost intensity after correction (column B, Table 1) averaged 5.6±1.4% for even-number interleaved EPI, vs. a slightly worse 6.8% for odd-number interleaved EPI. Figure 5 shows the uncor-

Table 1
Ghost Correction Results

Experiment	Matrix size of combined data set	Number of interleafs	A Ghost intensity before correction	B Ghost intensity after correction	C Percent reduction in ghost intensity	D Phase distortion estimate across FOV from linear fit	E Average residual of phase distortion estimate from linear fit	F Average standard deviation of y-dependent phase distortion estimates
Simulation: No distortion	256 × 256	16	0.5%	0.5%	0.1%	0.028	0.025	0.154
Simulation: 1.013 echo delay	256 × 256	16	50.3%	0.6%	98.8%	182.4	0.026	0.154
Phantom	128 × 128	4	10.2%	4.3%	57.9%	86.4	1.59	4.42
Phantom	256 × 256	8	17.0%	7.1%	58.0%	110.5	3.47	4.75
Phantom	256 × 256	16	13.4%	5.5%	58.9%	126.1	3.32	4.29
Phantom	256 × 256	9	37.2%	6.8%	81.8%	105.2	0.90	12.87
Head	128 × 128	4	10.5%	5.8%	44.7%	99.7	1.28	4.30
Head	256 × 256	8	15.1%	9.2%	39.2%	100.3	3.86	5.50
Head	256 × 256	16	9.3%	6.4%	31.2%	119.3	4.84	5.36
Head	256 × 256	9	34.6%	11.1%	67.9%	110.1	2.33	5.81
Head: A/P phase	256 × 256	8	10.2%	7.3%	28.1%	95.8	4.37	6.90
Head: A/P phase	256 × 256	9	32.6%	8.1%	75.3%	96.6	1.75	3.51

Ghost intensity, before and after correction, is measured relative to average intensity of corresponding parent image. Phase distortion measurements are in degrees. “1.013 echo delay” is in units of sampling interval. It refers to the difference in echo center between forward and reverse echos. “. . . Across FOV” refers to the difference in the phase distortion between the extreme right and left of the FOV in the frequency encode direction. “Residual of phase distortion estimates from linear fit” refers to the absolute value of the difference between the estimate and the linear fit approximation. “Y-dependent phase distortion estimates” refers to the variability of individual estimates at different y locations, for each x location. In the last two columns, averages are taken across x locations.

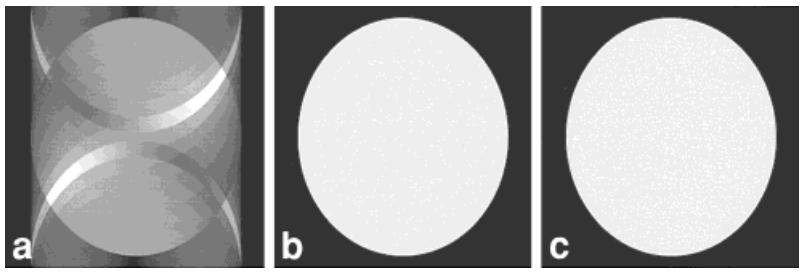

FIG. 3. Computer simulation using 16-interleaf EPI with a 1.013 sample interval relative echo center delay between left-to-right and right-to-left lines of *k*-space: **a:** Uncorrected reconstruction. **b:** Corrected reconstruction. Ghost intensity was reduced from 50.3% of the parent image intensity in the uncorrected image to 0.6% of the parent image intensity in the corrected image. **c:** Reconstruction with ghost correction using data with no phase distortion. The corrected image (**b**) was equal in quality to image (**c**).

rected and corrected axial brain images using (a) 4, (b) 16, (c) 8, and (d) 9-interleaf axial EPI acquisitions, with phase encoding in the R/L direction. Ghost intensity after correction averaged 7.1±1.8% for even-number interleaved EPI, vs. a worse 11.1% for odd-number interleaved EPI. Figure 6 shows the original and corrected reconstructed head images using (a) 8- and (b) 9-interleaf axial EPI acquisitions, with phase encoding in the A/P direction. Ghost intensity after correction was 7.3% with 8-interleaf EPI, vs. a slightly worse 8.1% with 9-interleaf. Figure 7 graphs the phase distortion estimates and related data obtained from the 8-interleaf EPI axial head scan (Fig. 5c).

Simulation

Figure 8a graphs number of eligible pixels, N_e, vs. object size and number of interleaves h. Figure 8b gives the total signal $|W|$, (W defined above Eq. [11]) as a function of object size and h. $|W|$ is low for small and large object sizes, and independent of h. The odd-number interleaved EPI yields the largest $|W|$ for object sizes of one-quarter to three-fourths of the FOV. When the object size is half the FOV, $|W|$ is twice that obtained with any even-number interleaved EPI. $|W|$ is relatively independent of h, provided h is even. Figure 8c and d show σ_W^2 for different $|W|$, h and object size, and demonstrate that σ_W^2 is independent of h and object size. The linear fit of σ_W^2 to $|W|$, h and object size shows that $\sigma_W \propto |W|^{1/2}$. It follows that $\sigma_\theta \propto |W|^{-1/2}$. Figure 8 is applicable to any number of pixels N in the phase-encode direction. Object size can be written from 0 to 1, as a fraction of the FOV, and $|W|$ can be written relative to the maximum for a uniform unit-intensity object, which is $N/8$ for a reconstruction of size N. The number of interleaves remains as given.

DISCUSSION

This paper provides the first successful image-based correction of multiple, closely-spaced ghosts generated in general interleaved EPI. Images reconstructed from non-alternating *k*-space patterns, obtained using even- or odd-number interleaved EPI, can be corrected just as well as images reconstructed from alternating *k*-space patterns obtained using single-shot or odd-number interleaved EPI. Ghost correction greatly improved image quality both outside and within the parent image. With correction, the appearance of artifactual image intensity variations, blurred and replicated tissue boundaries, and replicated tissue structures within the parent image, were consistently and substantially reduced (e.g., compare visual cortex regions in Fig. 5, especially b).

Column D of Table 1 lists the total phase distortion across the FOV in each scan. Phase distortions were 107.0±14.2° for the phantom studies, 107.3±8.1° for the axial head studies, and 96.2±0.4° for the axial head studies with AP phase encoding. These similar values indicate that system behavior was consistent and not a confounding factor in data interpretation. Column F gives the average, over x locations, of the standard deviation of θ_0 across y locations. This value estimates the error that would be obtained if only one pixel were used to estimate the phase distortion at each x. For the phantom images, the standard deviations of θ_0 for even-number interleaved EPI were 4.49±0.24°, i.e., 4.42° for the 4-interleaf, 4.75° for the 8-interleaf, and 4.29° for the 16-interleaf EPI. For the axial head images, the standard deviations were 5.06±0.66°. The 8-interleaf EPI with AP encoding shows a slightly higher 6.90°. These data agree with simulation results in Fig. 8, which shows that $|W|$ is essentially independent of h (for any even h) for a given object size, and decreases as the object size approaches the FOV. While the standard deviation of θ_0 using the 9-interleaf EPI axial head images was consistent with simulation results (i.e., same or better than the even-number interleaved EPI), the 9-interleaf EPI images of the phantom had a much higher than expected standard deviation. This was found to be due to the plastic grid within the phantom. This grid caused M_l and M_r to be of low intensity at many eligible pixels, producing high variability in θ_0. In regions with adequate signal intensity, the standard deviation was 8.5°, slightly better than that obtained with even-number interleaved EPI, as expected. Low signal did not occur with any even-number interleaved EPI phantom images, due to multiple overlapping ghosts. It is important to point out that Column F values do not estimate σ_θ, which is defined as the standard deviation of θ_0 obtained from Eq. [11]. Eq. [11] uses a sum over eligible pixels in which terms are weighted according to the intensity of M_l and M_r. The standard deviation of θ_0 reported in column G includes θ_0s from all eligible pixels, equally weighted. Column E gives the average residual of θ_0 from a linear fit across x. These residuals are consistently less than the standard deviations in column F. This reveals that it is advantageous to use linear fitting across x to improve the estimate, if only one pixel is used.

Hennel (15) found that in general interleaved EPI, the signal intensity of M_l and M_r in the ghost region is too low for reliable estimation of the phase distortion. This finding was based upon using only one pixel along the edge of the

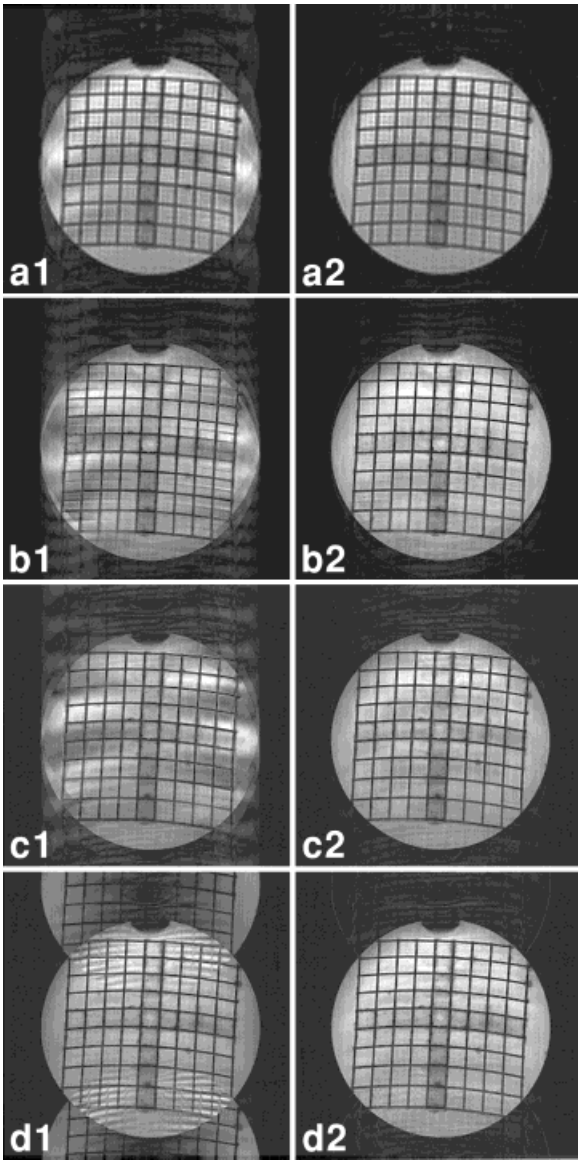

FIG. 4. Uncorrected (labeled with "1" after letter) and corrected (labeled with "2" after letter) axial reconstructions of a test phantom from 4, 16, 8, and 9-interleaf EPI acquisitions, with phase encoding in the R/L direction and standard *k*-space traversal pattern. **a:** 128 × 128 matrix using 4 interleaves of 128 × 32 each, with effective TE of 40 msec. **b:** 256 × 256 matrix using 16 interleaves of 256 × 16 each, with effective TE of 45.5 msec. **c:** 256 × 256 matrix was acquired using 8 interleaves of 256 × 32 each, with effective TE of 57.5 msec. **d:** 256 × 256 matrix was acquired using 9 interleaves of 256 × 28 each, with effective TE of 67.2 msec. Quality of ghost correction was slightly better with even-number interleaved EPI compared to odd-number. Ghost intensity after correction was 5.6±1.4% of parent image with even-number interleaved EPI, vs. 6.8% with the odd-number. Percent reduction of ghost intensity was much better with odd-number interleaved EPI; 81.8% vs. 58.3±0.5% with even-number.

image for the estimation. Our analysis shows that standard deviation of θ_o improves dramatically as the number of pixels used for the estimation is increased. This improvement is the main reason for the superiority of the present method to that in Ref. 15. Hennel (15) derived an identical expression for the phase distortion estimate from a single pixel (Eq. [10]) but did not derive its generalization for the estimate from multiple pixels. It is not unusual for the object to occupy only 75% of the FOV in the phase-encode direction. If a 64 matrix is acquired, then the standard

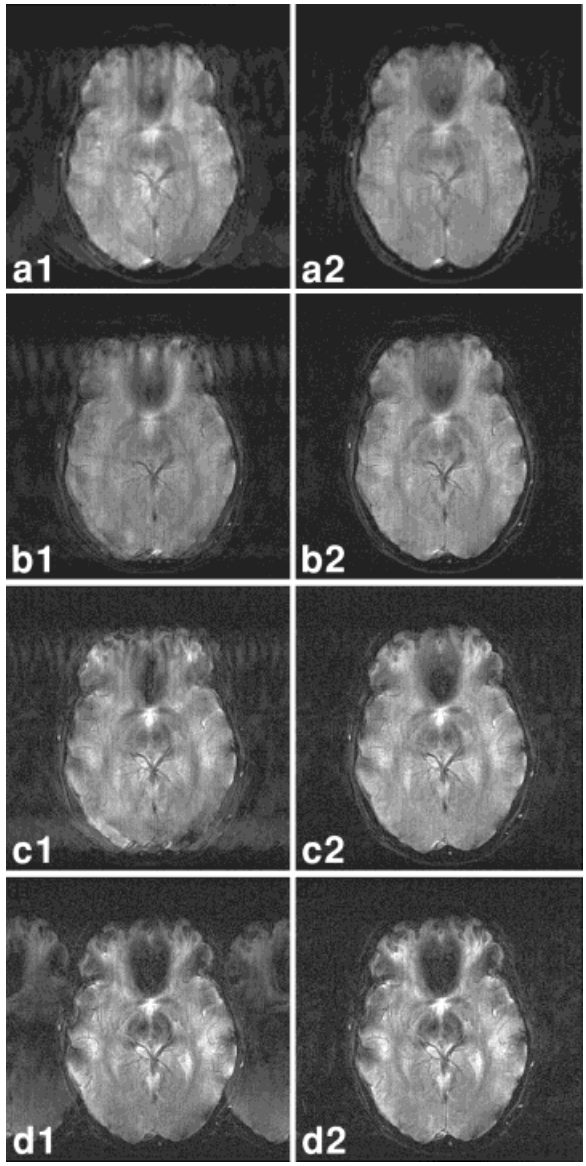

FIG. 5. Uncorrected (labeled with "1" after letter) and corrected (labeled with "2" after letter) axial reconstructions of the human brain in a normal subject, from 4, 16, 8, and 9-interleaf EPI acquisitions, with phase encoding in the R/L direction and standard *k*-space traversal pattern**. a:** 128 × 128 matrix using 4 interleaves of 128 × 32 each, with effective TE of 40 msec. **b:** 256 × 256 matrix using 16 interleaves of 256 × 16 each, with effective TE of 45.5 msec. **c:** 256 × 256 matrix was acquired using 8 interleaves of 256 × 32 each, with effective TE of 57.5 msec. **d:** 256 × 256 matrix was acquired using 9 interleaves of 256 × 30 each, with effective TE of 67.2 msec. Quality of ghost correction was better with even-number interleaved EPI compared to odd-number. Ghost intensity after correction was 7.1±1.8% of parent image with even-number interleaved EPI, vs. 11.1% with the odd-number. Percent reduction of ghost intensity was better with odd-number interleaved EPI: 67.9% vs. 38.4±6.8% with even-number.

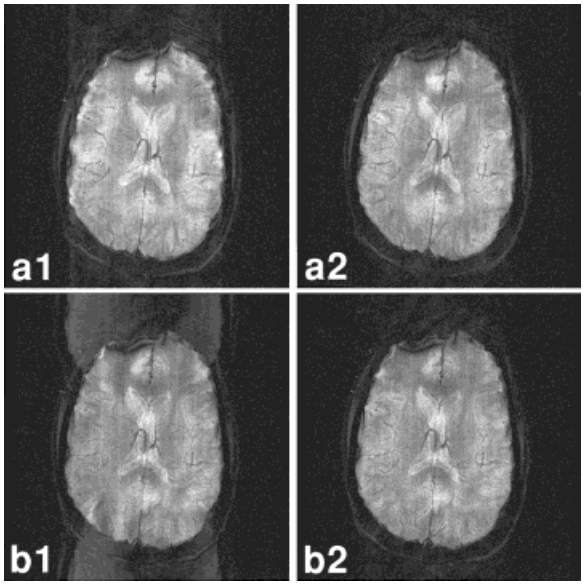

FIG. 6. Uncorrected (labeled with "1" after letter) and corrected (labeled with "2" after letter) axial reconstructions of the human brain in a normal subject, with phase encoding in the A/P direction and standard *k*-space traversal pattern**. a:** 256 × 256 matrix was acquired using 8 interleafs of 256 × 32 each, with effective TE of 57.5 msec. Ghost intensity after correction was 11.1% of the parent image intensity. **b:** 256 × 256 matrix was acquired using 9 interleafs of 256 × 28 each, with effective TE of 67.2 msec. Quality of ghost correction was slightly better with even-number interleaved EPI compared to odd-number. Ghost intensity after correction was 7.3% of parent image with even-number interleaved EPI, vs. 8.1% with the odd-number. Percent reduction of ghost intensity was much better with odd-number interleaved EPI; 75.3% vs. 28.1% with even-number.

deviation of the phase distortion estimate is improved by a factor of 4 if all the eligible pixels are used, rather than only one. In Ref. 15, the low SNR from one pixel was compensated for with a linear fit of the phase distortion over *x*, but that is not necessary when sufficient numbers of eligible pixels are used.

Computer simulation validated the experimental result that even-number interleaved EPI, which generated multiple ghosts, could be corrected just as well as odd-number interleaved EPI, which generated only one ghost. It showed that there is little dependence of σ_θ on h, for objects close in size to the FOV. In even-number interleaved EPI, the individual ghosts are low intensity, but all contribute to the eligible pixels and the total intensity is equal to that obtained with odd-number interleaved EPI. Computer simulation also validated the finding in Ref. 15 that the total signal from a single pixel for estimating the phase distortion is extremely low. In the simulation, $|W|$ from a single pixel was 0.25, corresponding to 0.5 signal from each of M_l and M_r (which are multiplied together in W). For objects nearly equal in size to the FOV, W increases linearly with N_e, and σ_θ varies as $N_e^{-1/2}$. Using all the eligible pixels, typical available signal in this simulation typically reached 4.0 (using an object size of 64 pixels), 16 times more than using one pixel.

A user-defined ROI is required to identify eligible pixels in each image. In practice, it is not necessary to draw an ROI for every image of the time-series, even if the subject's head moves slightly during the scan. Drawing the ROI slightly larger than the head is advised to reduce errors stemming from the Gibbs artifacts, which effectively extends the object size, and from voxel content changes at the brain edge due to subject motion. Drawing the larger ROI degrades performance slightly by reducing the number of eligible pixels. When the parent image is amidst a large number of closely spaced ghosts (e.g., 16 or 32), the edge can be difficult to track. Normal brain intensity variations, combined with relatively high-intensity ghosts, render off-the-shelf edge-detection programs useless. The development and validation of a program for general detection of the edge is a challenge and project in itself.

Foxall et al. (19) described an iterative method, for single-shot EPI only, that provides ghost correction equal in quality to that obtained using the exact solutions proposed in this study and in Ref. 1. Our formulation generalizes this method for interleaved EPI ghost correction. Eqs. [3] and [6] together generalize Eq. [1] of Ref. 19, and Eqs. [A.13] and [A.14] generalize Eqs. [6a] and [6b]. Both Ref. 19 and this study use a cost function for iterating and improving upon the phase distortion estimate. However, one of the key advantages of Ref. 19 is the use of a special cost function, which eliminates the requirement of a user-defined ROI to define "non-overlapping" pixels (pixels inside the ghost but outside the parent). We have not been

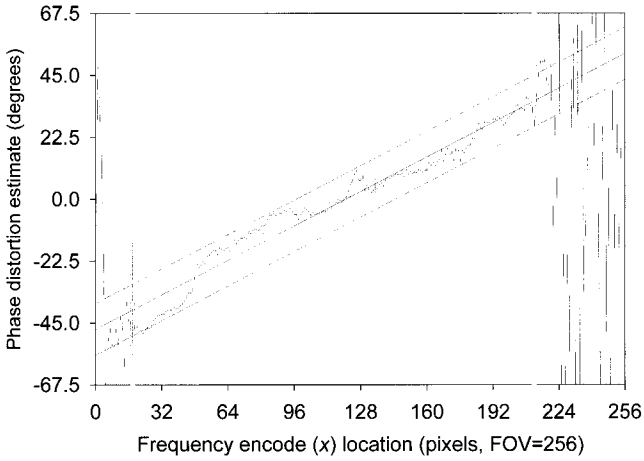

FIG. 7. This graph is obtained from the correction of the 8-interleaf EPI axial head acquisition with phase encoding in the R/L direction (refer to Fig. 5). All 256 locations along the frequency-encode direction are graphed. Gray vertical bars, crossing the horizontal axis (*x* location) at 18 and 212, show the extent of the brain tissue, and the range used for least-squares linear regression. The jagged line represents the phase distortion estimate θ_0 across *x*. At each *x*, the vertical error bar marks ±1 standard deviation of this phase distortion estimate across *y*. The average across *x* of this standard deviation is 5.50°, as listed in column F of Table 1. Outside of the object in the frequency-encode direction, where signal intensity was very low, the phase angle distortion estimates varied widely as a function of *y*, and the resulting phase distortion estimates had no recognizable trend. The linear least-squares fit to the data within the head is shown as a solid black line, with 95% confidence intervals shown with dashed lines. The phase distortion was 100.3° across the entire FOV (0.56° per pixel). The average residual error of θ_0 (absolute value) of the least squares fit across *x* was 3.86°.

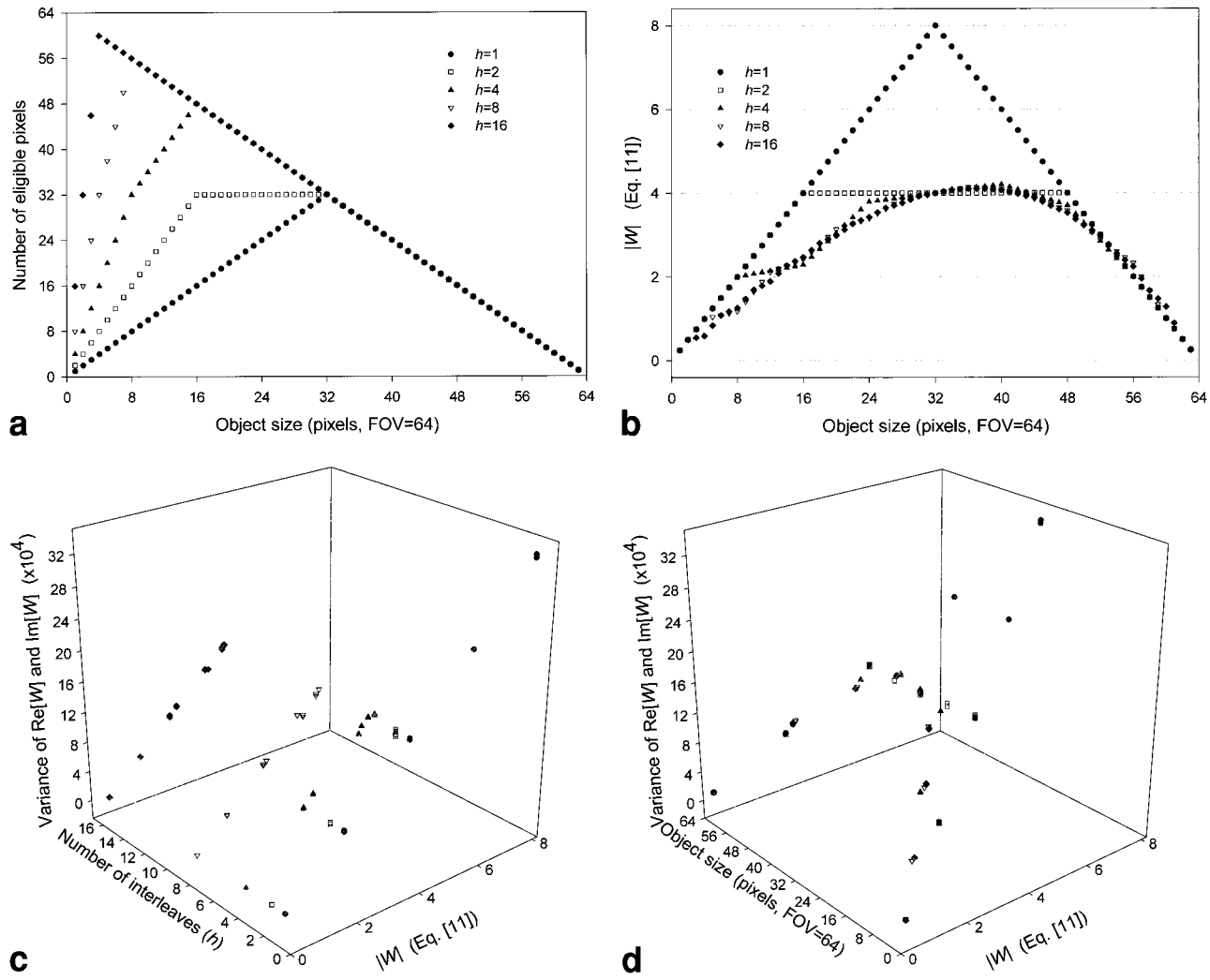

FIG. 8. Graphs were obtained from computer simulation of phase distortion estimation in the presence of random noise, based on 64-point reconstructions in the phase encode direction. Simulations used $h = 1$ (●), $h = 2$ (□), $h = 4$ (▲), $h = 8$ (▽) and $h = 16$ (♦). One run of 2000 instances of random noise, for object sizes 1, 8, 16, 24, 32, 40, 48, 56, and 63 and each h, were performed (45 runs in all). **a:** Number of eligible pixels (N_e) for each object size and h. Eligible pixels are locations outside of the parent image at which there is non-zero M_l and M_r. When parent image and ghosts do not overlap there are $2h$ formal ghost locations but the number of eligible pixels is h. Pixels shifted by an even-number of ghost separation intervals (Δ_1) are eligible pixels only if the ghosts shifted by an odd number of intervals are large enough to overlap that region. **b:** W from Eq. [11], assuming that object has uniform intensity one, for all object sizes 1 through 63 and all h. **c:** Plot and fit of the estimates of the variances of the real (Re) and imaginary (Im) parts of W (both denoted by σ_W^2 in text) to a linear function of $|W|$ and h. Graph demonstrates that σ_W, and hence σ_θ, is determined from $|W|$ alone; it is not dependent upon h. **d:** Plot and fit of σ_W^2 estimate to $|W|$ and object size demonstrates that σ_W is also not dependent upon the object size. In **c** and **d**, differences between the estimates of the variance of Re[W], and the variance of Im[W], for any given $|W|$, h and object size, were less than 1% of their mean. These differences are either not discernable or are barely discernable on the graph.

able to find a generalization of this cost function for general interleaved EPI. However, Foxall et al. (19) acknowledge that even though their method does not require the user-defined ROI, their ghost correction method is more accurate when one is available to select the non-overlapping pixels.

Our derivation provided an iterative method for estimating the phase distortion as a general function of x and y, i.e., $\theta(x,y)$. This iterative method was evaluated with Mathematica 4.0 (Wolfram Research, Inc., Urbana, IL), using the same simulation parameters described above, with up to four terms in the Taylor expansion in y of $\theta(x,y)$ for each x (i.e., $K_\theta = 1, 2, 3,$ or 4). With prescribed y dependence to distort the simulated raw data, the FindMinimum function was used to iterate between Eqs. [6] and [7]. This function always found the global solution having cost function equal to zero. It confirmed that the method was mathematically correct. However, the global solution was found only if the initial guess was relatively close to it. The function was often trapped in a local minimum of the cost function. The difficulty in achieving global minimization led us to regard the application of this iterative method as a separate project.

The experimental data did not show exact correspondence with all predictions of the theoretical model and

computer simulation. For example, the average object size in the axial head images with R/L encoding was about 50% percent of the FOV. Based upon Fig. 8, the θ_0 standard deviation for these images (Table 1, column F) should have been about $\sqrt{2}$ factor smaller with the 9-interleaf EPI, but in our examples the results were slightly worse. Exact correspondence cannot be expected, because important deviations from the theoretical model and computer simulation exist in the physical MRI system. These include other sources of ghosting which do not fit our original signal model, and the interaction with main field inhomogeneity. Other aspects of the experimental data were not predicted by theory or simulation. For example, the linear fit of θ_0 across x was much better with the 9-interleaf EPI compared to any of the even-number interleaved EPI sequences. There is a trend toward improved linearity of θ_0 across x with decreasing number of interleaves (taking $h = 1$ for 9-interleaf EPI). The physical mechanism whereby greater linearity across x might be generated is not known.

The proposed method is applicable to any pulse sequence in which the acquisition of k-space lines can be separated into left-to-right and right-to-left traversals. For example, the gradient and spin echo (GRASE) technique (20) combines spin echos and gradient-recalled echos in a single shot or interleaved sequence. Each 180° RF pulse acts to time-reverse the spin evolution, and the k-space line after the RF pulse will have the same acquisition direction as the line before it (since gradient polarity of the subsequent readout would remain the same). Acquisitions from successive gradient echos will have opposite direction. It is possible that the GRASE sequence will generate more than two classes of k-space lines, i.e., not simply left-to-right or right-to-left dependency, but also dependency on the temporal position of the lines relative to the RF pulses. The current method cannot be applied directly, but most likely can be adapted to this case.

In this study, even-number interleaved EPI was used for generating non-alternating k-space patterns, while odd-number interleaved EPI was used for generating alternating k-space patterns. A more direct comparison of ghost correction for alternating and non-alternating k-space patterns would have been obtained using only odd-number interleaved EPI. This was not done because the odd-number interleaved EPI is relatively new and not widely used, and in practice is used only for generating the alternating pattern. Hennel (15) had already demonstrated both theoretically and experimentally that the quality of ghost correction for non-alternating k-space patterns is determined by the number of interleaves, and not particularly on whether the number of interleaves is even or odd. The even-number EPI is widely used, and generates non-alternating patterns. Its use in this study makes the results more relevant and important for current interleaved EPI users.

APPENDIX

Signal and Image Equations

Let N equal the number of data points in the k_x and k_y directions and in the final image. Define $g_{lr}(n)$ according to the direction of the nth k-space line,

$$g_{lr}(n) = \begin{cases} 1 \;\; \textit{if } n\text{th k-space line acquired from left to right} \\ \qquad (\text{“left-to-right echo”}) \\ -1 \;\; \textit{if } n\text{th k-space line acquired from right to left} \\ \qquad (\text{“right-to-left echo”}) \end{cases} \quad [A.1]$$

Define $\theta_l(x,y)$ and $\theta_r(x,y)$ as the phase distortion at each echo center for left-to-right and right-to-left echos, respectively. Set the spatial scale such that the object being reconstructed, $M(x,y)$, is defined at $N \times N$ integer-valued points in the spatial domain. Then the conjugate spatial and frequency variables can be regarded as dimensionless, and the signal S is defined at points labeled by integers (m,n) in k-space (1). The inverse discrete Fourier transform (inverse DFT) applied to S produces the reconstructed image $\hat{M}(x,y)$ given by

$$\hat{M}(x, y) = M_l(x, y) + M_r(x, y) \quad [A.2]$$

with $M_l(x,y)$ reconstructed from only the left-to-right echos and $M_r(x,y)$ from only the right-to-left echos. These images are given by

$$M_l(x, y) = \frac{1}{2} M(x, y)\exp(i\theta_l(x, y)) + \frac{1}{2i} \sum_{j=0}^{2h-1} g_j M(x, y - \Delta_j)\exp(i\theta_l(x, y - \Delta_j))$$

$$M_r(x, y) = \frac{1}{2} M(x, y)\exp(i\theta_r(x, y)) - \frac{1}{2i} \sum_{j=0}^{2h-1} g_j M(x, y - \Delta_j)\exp(i\theta_r(x, y - \Delta_j)) \quad [A.3]$$

where $\Delta_j \equiv j\,N/2h$ and g_j identify each ghost location and complex amplitude factor, respectively. The $g_{lr}(n)$ and g_j are related by

$$g_{lr}(n) = -i \sum_{j=0}^{2h-1} g_j \exp\left(i \frac{2\pi}{N} n\Delta_j \right)$$

$$g_j = (i/2h) \sum_{n=0}^{2h-1} g_{lr}(n)\exp\left(-i \frac{2\pi}{N} n\Delta_j \right) \quad [A.4]$$

as derived in Ref. 16. To write Eq. [A.3] in a matrix form needed for algorithm development, define column vectors $\vec{M}(x,y)$, $\vec{M}_l(x,y)$, and $\vec{M}_r(x,y)$ of length $2h$ with entries,

$$[\vec{M}(x, y)]_j \equiv M(x, y - \Delta_j) \quad [\vec{M}_l(x, y)]_j \equiv M_l(x, y - \Delta_j) \quad [A.5]$$

$$[\vec{M}_r(x, y)]_j \equiv M_r(x, y - \Delta_j)$$

Eq. [A.3] may now be written

$$\vec{M}_l(x, y) = \frac{1}{2}(I + C)\exp(i\Theta_l(x, y))\vec{M}(x, y) \quad [A.6]$$

$$\vec{M}_r(x, y) = \frac{1}{2}(I - C)\exp(i\Theta_r(x, y))\vec{M}(x, y)$$

where I is a $2h \times 2h$ identity matrix, $\Theta_l(x,y)$ is a $2h \times 2h$ diagonal phase distortion matrix given by

$$[\Theta_l(x, y)]_{i,j} \equiv \theta_l(x, y - \Delta_j) \quad if\ i = j, \quad 0\ otherwise \quad [A.7]$$

and similarly for $\Theta_r(x,y)$, and C is a $2h \times 2h$ circulant matrix with $[C]_{j,n} \equiv g_{j-n}$. Defining discrete Fourier transform matrices $\underset{\sim}{U}$ by $[\underset{\sim}{U}]_{j,n} \equiv \frac{1}{2h}\exp\left(i\frac{\pi}{h}jn\right)$, where $j = 0,1,\ldots,2h-1$, and $n = 0,1,\ldots,2h-1$, the circulant matrix can be diagonalized according to $\Lambda = \underset{\sim}{U}\, C\, \underset{\sim}{U}^{-1}$, where Λ is $[\Lambda]_{n,j} = \lambda_n$ if $n = j$, 0 otherwise. Define $\vec{g}_{lr}$, $\vec{g}$ and $\vec{\lambda}$ as column vectors of length $2h$ with entries $[\vec{g}_{lr}]_n \equiv g_{lr}(n)$, $[\vec{g}]_j \equiv g_j$, and $[\vec{\lambda}]_j \equiv \lambda_j$. The relationships between $g_{lr}(n)$, λ_n, and g_j are $\vec{\lambda} = (2h)\underset{\sim}{U}\vec{g}$, $\vec{g}_{lr} = (2h)\underset{\sim}{U}\vec{g}$ and $\vec{\lambda} = \vec{g}_{lr}$. Eq. [A.6] can now be rewritten in terms of Λ using the projection matrix $\underset{\sim}{P}_0 \equiv \frac{1}{2}(I + \Lambda)$, where $\underset{\sim}{P}_0$ and $(I - \underset{\sim}{P}_0)$ have equal numbers of 0 and 1 entries along the diagonal, and obey $\underset{\sim}{P}_0(I - \underset{\sim}{P}_0) = 0$. Regardless of the specific pattern of k-space lines, the vector $\vec{g}_{lr}$ has an equal number (h) of +1 and –1 entries. Without loss of generality, it can be assumed that $\vec{g}_{lr}$ is of the form $\vec{g}_{lr} = (1\,1\cdots1\,-1\,-1\cdots-1)^{\mathrm{T}}$, where T denotes transpose, corresponding to the typical non-alternating pattern of left-to-right and right-to-left echos. For other patterns, a reordering matrix T is defined to switch rows and columns to put the matrices into this standard form. Define transformation matrices U and U^{-1} that include the effect of reordering, as $U = \underset{\sim}{U}T$, and $U^{-1} = T\underset{\sim}{U}^{-1}$. From Eq. [A.6], the transformed $\vec{M}_l(x,y)$ and $\vec{M}_r(x,y)$ are given by

$$\vec{M}_l(x, y) = UP_0U^{-1}\exp(i\Theta_l)\vec{M}$$

$$\vec{M}_r(x, y) = U(I - P_0)U^{-1}\exp(i\Theta_r)\vec{M} \quad [A.8]$$

Ghost Correction Matrix Equations

The unknown $\vec{M}(x,y)$ must be eliminated from the right sides of Eq. [A.8] to obtain an implicit equation for the unknowns $\Theta_l(x,y)$ and $\Theta_r(x,y)$. The matrix equation is partitioned into two blocks (denoted by superscripts (1) and (2) of h elements each, using the definitions:

$$\vec{M}(x, y) \equiv \begin{pmatrix} \vec{M}^{(1)}(x, y) \\ \vec{M}^{(2)}(x, y) \end{pmatrix} \quad \vec{M}_l(x, y) \equiv \begin{pmatrix} \vec{M}_l^{(1)}(x, y) \\ \vec{M}_l^{(2)}(x, y) \end{pmatrix}$$

$$\vec{M}_r(x, y) \equiv \begin{pmatrix} \vec{M}_r^{(1)}(x, y) \\ \vec{M}_r^{(2)}(x, y) \end{pmatrix} \quad [A.9]$$

The transformation matrices are partitioned into 2×2 blocks of $h \times h$ matrices according to

$$U \equiv \frac{1}{2h}\begin{pmatrix} U_{11} & U_{12} \\ U_{21} & U_{22} \end{pmatrix} \quad U^{-1} \equiv \begin{pmatrix} U_{11}^H & U_{12}^H \\ U_{21}^H & U_{22}^H \end{pmatrix} \quad [A.10]$$

and the phase distortion matrix $\Theta_l(x,y)$ is partitioned according to

$$\Theta_l(x, y) \equiv \begin{pmatrix} \Theta_l^{(1)}(x, y) & 0 \\ 0 & \Theta_l^{(2)}(x, y) \end{pmatrix} \quad [A.11]$$

and similarly for $\Theta_r(x,y)$. Projection matrices defined by $P_0 \equiv T\,\underset{\sim}{P}_0\,T$ and $I - P_0 \equiv T(I - \underset{\sim}{P}_0)T$ are

$$P_0 \equiv \begin{pmatrix} I & 0 \\ 0 & 0 \end{pmatrix} \quad I - P_0 = \begin{pmatrix} 0 & 0 \\ 0 & I \end{pmatrix}. \quad [A.12]$$

Using these, Eq. [A.8] can be partitioned as

$$\begin{pmatrix} \vec{M}_l^{(1)} \\ \vec{M}_l^{(2)} \end{pmatrix} = \frac{1}{2h}\begin{pmatrix} U_{11} & U_{12} \\ U_{21} & U_{22} \end{pmatrix}\begin{pmatrix} I & 0 \\ 0 & 0 \end{pmatrix}\begin{pmatrix} U_{11}^H & U_{12}^H \\ U_{21}^H & U_{22}^H \end{pmatrix} \uparrow \times \begin{pmatrix} \exp(i\Theta_l^{(1)}) & 0 \\ 0 & \exp(i\Theta_l^{(2)}) \end{pmatrix}\begin{pmatrix} \vec{M}^{(1)} \\ \vec{M}^{(2)} \end{pmatrix} \quad [A.13]$$

and

$$\begin{pmatrix} \vec{M}_r^{(1)} \\ \vec{M}_r^{(2)} \end{pmatrix} = \frac{1}{2h}\begin{pmatrix} U_{11} & U_{12} \\ U_{21} & U_{22} \end{pmatrix}\begin{pmatrix} 0 & 0 \\ 0 & I \end{pmatrix}\begin{pmatrix} U_{11}^H & U_{12}^H \\ U_{21}^H & U_{22}^H \end{pmatrix} \uparrow \times \begin{pmatrix} \exp(i\Theta_r^{(1)}) & 0 \\ 0 & \exp(i\Theta_r^{(2)}) \end{pmatrix}\begin{pmatrix} \vec{M}^{(1)} \\ \vec{M}^{(2)} \end{pmatrix}. \quad [A.14]$$

Consider the unknown results on the right sides of Eqs. [A.13] and [A.14], just preceding the multiplication by zero in P_0 and $I - P_0$ (marked with vertical arrow). At that position, the upper vector element in Eq. [A.13] is $U_{11}^{-1}\vec{M}_l^{(1)}$ and the lower vector element in Eq. [A.14] is $U_{22}^{-1}\vec{M}_r^{(2)}$. Note that the lower vector element in Eq. [A.13] on the left side equals zero, and the first vector element in Eq. [A.14] on the left side equals zero. Let $U_{12}^{-1}X_l$ and $U_{21}^{-1}X_r$ denote the corresponding unknown vectors at the arrow position. With left multiplication by U, Eqs. [A.13] and [A.14] become, respectively,

$$\frac{1}{2h}\begin{pmatrix} I & I \\ U_{21}U_{11}^{-1} & U_{22}U_{12}^{-1} \end{pmatrix}\begin{pmatrix} \vec{M}_l^{(1)} \\ X_l \end{pmatrix} = \begin{pmatrix} \exp(i\Theta_l^{(1)})\vec{M}^{(1)} \\ \exp(i\Theta_l^{(2)})\vec{M}^{(2)} \end{pmatrix} \quad [A.15]$$

and

$$\frac{1}{2h}\begin{pmatrix} U_{11}U_{21}^{-1} & U_{12}U_{22}^{-1} \\ I & I \end{pmatrix}\begin{pmatrix} X_r \\ \vec{M}_r^{(2)} \end{pmatrix} = \begin{pmatrix} \exp(i\Theta_r^{(1)})\vec{M}^{(1)} \\ \exp(i\Theta_r^{(2)})\vec{M}^{(2)} \end{pmatrix} \quad [A.16]$$

These are now combined to yield Eq. [6] in the main text, with unknowns X_l and X_r on the left side, and with $\Theta \equiv \frac{1}{2}(\Theta_l - \Theta_r)$. Corrected images $\vec{M}_C$, (defined in Eq. [3]) are obtained from Eqs. [A.15], [A.16], and Eq. [6] (to derive X_l and X_r) to yield Eq. [4] in the main text.

Iterative Procedure to Estimate Θ

For each (x,y) location, Θ that minimizes Eq. [7] and simultaneously solves Eq. [6] can be regarded as an optimal phase distortion estimate. With Θ defined by Eq. [4], a series expansion, such as $\theta(x, y - k\Delta) \cong \theta_0 + (k\Delta)\theta_1 + \frac{1}{2}(k\Delta)^2\,\theta_2 + \ldots$ can be used to specify the unknowns in Θ for each location. A rigorous derivation of the number of unknowns permitted in Θ is lengthy and outside the scope of this paper, so only a short argument is provided. In Eqs. [A.15] and [A.16], replace Θ_l with Θ, and Θ_r with $-\Theta$ (to implement the phase difference dependence). Note that if there are no constraints on $M(x,y - k\Delta)$, Eqs. [A.15] and [A.16] represent *2h* equations and *4h* unknowns (*h* unknowns in X_l, *h* unknowns in X_r and *2h* unknowns in Θ). Let *K* denote the number of integers *k* for which $M(x,y - k\Delta) = 0$. These constraints reduce the number of unknowns in X_l to *h-K*, and in X_r to *h-K*. They also reduce the number of linearly independent equations to *2h-K*. Thus, to balance the number of equations and unknowns in Eqs. [A.15] and [A.16], only *K* variables in Θ are permitted. Let K_θ denote the number of unknowns actually used in Θ. Setting $K_\theta \le K$ will allow Eq. [6] to be solved with minimization of I in Eq. [7].

Closed-Form Solution to Estimate Θ

The special case $K = 1$ requires $K_\theta = 1$ (i.e., $\Theta^{(1)} = \theta_0\, I$ and $\Theta^{(2)} = \theta_0\, I$, $\theta_0\, I$, θ_0 scalar) and results in a closed-form solution. Eq. [6] becomes

$$\begin{pmatrix} U_{11}U_{21}^{-1} & I \\ I & U_{22}U_{12}^{-1} \end{pmatrix}\begin{pmatrix} \exp(i2\theta_0)X_r \\ -X_l \end{pmatrix} = \begin{pmatrix} I & U_{12}U_{22}^{-1} \\ U_{21}U_{11}^{-1} & I \end{pmatrix}\begin{pmatrix} \vec{M}_l^{(1)} \\ -\exp(i2\theta_0)\vec{M}_r^{(2)} \end{pmatrix} \quad [A.17]$$

and since the matrices are invertible, X_l and X_r can be solved, with the result given in Eq. [8]. Eq. [A.17] gives a familiar form (see, e.g., Refs. 15 and 19) for the corrected images, Eq. [9]. Making substitutions from Eq. [8], all squared magnitude terms in I (Eq. [7]) are seen to be independent of θ_0 and can be eliminated. Defining positive definite I′ without these terms yields

$$\mathrm{I}' = 2\ \mathrm{Re}[\exp(i2\theta_0)w] \quad [A.18]$$

where scalar *w* is defined below Eq. [10], and setting the derivative of I′ with respect to θ_0 equal to zero gives Eq. [10]. To average the phase distortion estimates found at different eligible *y* locations, introduce a *y* subscript to change I′ to I'_y, and define the sum $\mathbf{I}'$ over *y* locations as

$$\mathbf{I}' \equiv \sum_y \mathrm{I}'_y = 2\ \mathrm{Re}[\exp(i2\theta_0)W] \quad [A.19]$$

where scalar *W* is defined below Eq. [10]. Setting the differential of $\mathbf{I}'$ with respect to θ_0 equal to zero gives Eq. [11], the final result.

Correspondence With Solution in Ref. 15

Eq. [5] in Ref. 15 (the equation for $\exp(-i2\theta_0)$) shows that the phase distortion estimate θ_0 for location *x* is determined by the ratio of M_l and M_r at any single point outside the object. This expression is not immediately obtained from the iterative method represented by Eqs. [3], [6], and [7] in this paper. However, Eq. [5], as well as Eq. [12] (for $M_l(x,y)$) and Eq. [13] (for $M_r(x,y)$) in Ref. 15, can be derived directly from Eqs. [A.13] and [A.14]. Using $\Theta_l = \theta_0$ and $\Theta_r = -\theta_0$ and one obtains

$$\begin{pmatrix} \vec{M}_l^{(2)} \\ \vec{M}_r^{(2)} \end{pmatrix} = \begin{pmatrix} \exp(i\theta_0) & 0 \\ 0 & \exp(-i\theta_0) \end{pmatrix} \times \begin{pmatrix} U_{21}U_{11}^H & U_{21}U_{12}^H \\ U_{22}U_{21}^H & U_{22}U_{22}^H \end{pmatrix}\begin{pmatrix} \vec{M}^{(1)} \\ \vec{M}^{(2)} \end{pmatrix} \quad [A.20]$$

Using the identities derived from $UU^{-1} = I$, this becomes

$$\vec{M}_l^{(2)} = \exp(i\theta_0)Q_l^{(2)} \quad \vec{M}_r^{(2)} = \exp(-i\theta_0)(-Q_l^{(2)} + \vec{M}^{(2)}), \quad [A.21]$$

where $2hQ_l^{(2)} \equiv U_{21}U_{11}^H\vec{M}^{(1)} + U_{21}U_{12}^H\vec{M}^{(2)}$. At locations (x,y) where $M(x,y - k\Delta) = 0$ for some $k \ge h$, $[\vec{M}^{(2)}]_{k-h} = 0$ and Eq. [A.21] reduces to $-[M_r^{(2)}]_{k-h}/[M_l^{(2)}]_{k-h} = \exp(-2i\theta)$, which agrees with Eq. [5] in Ref. 15. The term $Q_l^{(2)}$ gives the coefficients A_m derived from the infinite series, Eq. [A7], in Ref. 15. Using Eqs. [A.13] and [A.14] with $M_l^{(1)}$ and $M_r^{(1)}$ yields

$$\vec{M}_l^{(1)} = \exp(i\theta_0)Q_l^{(1)} \quad \vec{M}_r^{(1)} = \exp(-i\theta_0)(-Q_l^{(1)} + \vec{M}^{(1)}), \quad [A.22]$$

where $2hQ_l^{(1)} \equiv U_{11}U_{11}^H\vec{M}^{(1)} + U_{12}U_{22}^H\vec{M}^{(2)}$. These are used to estimate the phase distortion when $[\vec{M}^{(1)}]_k = 0$, for some $0 \le k \le h - 1$. The first row of $\vec{M}_l^{(1)}$ and $\vec{M}_r^{(1)}$ in Eq. [A.22] are expressions for $M_l(x,y)$ and $M_r(x,y)$ that match Eqs. [12] and [13] in Ref. 15.

REFERENCES

1. Buonocore MH, Gao L. Ghost artifact reduction for echo-planar imaging using image phase correction. Magn Reson Med 1997;38:89–100.
2. McKinnon GC. Ultrafast interleaved gradient echo planar imaging on a standard scanner. Magn Reson Med 1993;30:609–616.
3. Butts K, Riederer SJ, Ehman RL, Thompson RM, Jack CR. Interleaved echo planar imaging on a standard MRI system. Magn Reson Med 1994;31:67–72.
4. Feinberg DA, Oshio K. Phase errors in multi-shot echo planar imaging. Magn Reson Med 1994;32:535–539.
5. Slavin GS, Butts K, Rydberg JN, Jack CR, Riederer SJ. Dual-echo interleaved echo-planar imaging of the brain. Magn Reson Med 1995;33:264–270.
6. Bruder H, Fischer H, Reinfelder HE, Schmitt F. Image reconstruction for echo planar imaging with nonequidistant *k*-space sampling. Magn Reson Med 1992;23:311–323.
7. Wong EC. Shim insensitive phase correction for EPI using a two echo reference scan. In: Proceedings of SMRM, 11th Annual Meeting, Berlin, Germany, 1992. p 4514.
8. Jesmanowicz A, Wong EC, Hyde JS. Phase correction for EPI using internal reference lines. In: Proceedings of SMRM, 12th Annual Meeting, New York, 1993. p 1239.
9. Maier JK, Vevrek M, Glover GH. Correction of NMR data acquired by an echo planar technique. US Patent #5,151,656; 1992.

10. Jesmanowicz A, Wong EC, Hyde JS. Self-correcting EPI reconstruction algorithm. In: Proceedings of the 3rd Annual Meeting of ISMRM, Nice, France, 1995. p 619.
11. Mandeville JB, Weisskoff RM, Garrido L. Reduction of eddy-current induced Nyquist ghosts and sampling artifact. In: Proceedings of the 3rd Annual Meeting of ISMRM, Nice, France, 1995. p 613.
12. Hu X, Le TH. Artifact reduction in EPI with phase encoded reference scan. Magn Reson Med 1996;36:166–171.
13. Reeder SB, Atalar E, Bolster BD, McVeigh ER. Quantification and reduction of ghosting artifacts in interleaved echo-planar imaging. Magn Reson Med 1997;38:429–439.
14. Clare S, Bowtell R, Morris P. Ghost artefact in fMRI: comparison of techniques for reducing the N/2 Ghost. In: Proceedings of the ISMRM, on CD-ROM, 1998. p 2137.
15. Hennel F. Image-based reduction of artifacts in multishot echo-planar imaging. J Magn Reson 1998;134:206–213.
16. Buonocore MH, Zhu DC. High spatial resolution EPI using an odd number of interleaves. Magn Reson Med 1999;41:1199–1205.
17. Buonocore MH, Perlmutter RJ, Kirk G, Shepp LA. A new analytic simulation method for magnetic resonance (MR) imaging. Poster. SMRM 4th Annual Meeting, London, Aug 16–20, 1985.
18. Bronstein J. Master's thesis. Biomedical engineering graduate program, UC Davis, June 1998.
19. Foxall DL, Harvey PR, Huang J. Rapid iterative reconstruction for echo planar imaging. Magn Reson Med 1999;42:541–547.
20. Feinberg DA, Johnson G, Kiefer B. Increased flexibility in GRASE imaging by *k*-space banded phase encoding. Magn Reson Med 1995;34: 149–155.